Probing dark photons in the early universe with big bang nucleosynthesis

Journal of Cosmology and Astroparticle Physics
An IOP and SISSA journal

Probing dark photons in the early universe with big bang nucleosynthesis

Jung-Tsung Li, George M. Fuller and Evan Grohs

JCAP12(2020)049

Abstract.

Keywords:

ArXiv ePrint:

JCAP12(2020)049

JCAP12(2020)049

JCAP12(2020)049

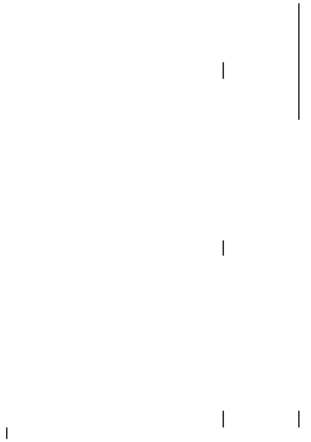

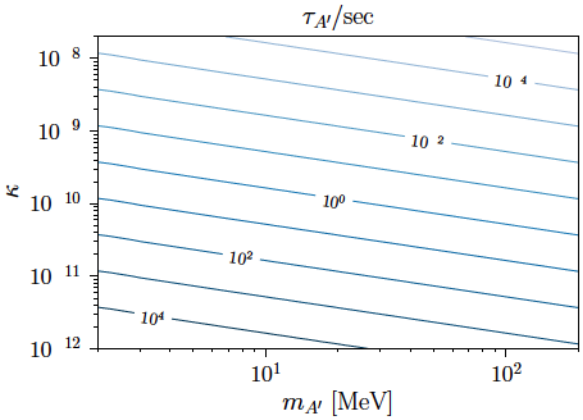

Figure 1. Contours of constant dark photon life time $\tau_{A'}$ (in seconds) as functions of κ and $m_{A'}$.

From the last term in equation (2.1), we see that the *effective* coupling between the dark photon $\tilde{A_\mu}'$ and the standard model electric charge current $J^\mu_{\rm em}$ is

$$e\kappa_{{\rm eff},a} = \frac{e\,\kappa\,m_{A'}^2}{\sqrt{\left(m_{A'}^2 - {\rm Re}\,\pi_a\right)^2 + \left({\rm Im}\,\pi_a\right)^2}}. \tag{2.2}$$

Certainly, the physics should be independent of the basis we choose. So in the following discussion, we will refer to the rotated (mass state) $\tilde{A}'$ as the dark photon and designate this simply as A'.

The physical meaning of the real and imaginary parts of π_a follows from considerations of finite temperature field theory. The real part can be interpreted as the effective photon mass in the plasma. With the polarization vectors chosen in equations (A.1) and (A.2), the dispersion relation for EM waves follows the form $\omega^2 = |\mathbf{k}|^2 + {\rm Re}\,\pi_a$ for $a = \pm{\rm T}$ and L.

The imaginary part of π_a describes the rate at which the non-equilibrium dark photon distribution function evolves toward thermal equilibrium. Quantitatively, it is ${\rm Im}\,\pi_a = -\omega(\Gamma^{\rm abs}_{A_a} - \Gamma^{\rm prod}_{A_a})$, where $\Gamma^{\rm abs}_{A_a}$ and $\Gamma^{\rm prod}_{A_a}$ denote the absorption rate and spontaneous production rate, respectively [38]. In a local thermal (steady state) equilibrium, detailed balance would dictate that $\Gamma^{\rm prod}_{A_a} = e^{-\omega/T}\Gamma^{\rm abs}_{A_a}$.

Specifically, $\Gamma^{\rm prod}_{A_a}$ in this work denotes the annihilation rate for lepton or quark pairs into one SM photon and is evaluated as (see appendix C)

$$\Gamma^{\rm prod}_{A_a}(\omega) = \frac{1}{2\omega}\int \frac{d^3\mathbf{p}}{(2\pi)^3\,2E_{\mathbf{p}}}\,\frac{d^3\mathbf{q}}{(2\pi)^3\,2E_{\mathbf{q}}}\,\frac{1}{e^{E_{\mathbf{p}}/T}+1}\,\frac{1}{e^{E_{\mathbf{q}}/T}+1} \times \sum_{\rm spin}|\mathcal{M}_{l\bar{l}\to A_a}|^2\,(2\pi)^4\,\delta^{(4)}\left(k-p-q\right), \tag{2.3}$$

where $\mathcal{M}_{l\bar{l}\to A_a}$ is the matrix element for lepton-pair (momenta $\mathbf{p}$ and $\mathbf{q}$) annihilation to one vector boson through a standard EM vertex and the sum is over initial lepton spin states. As a result, the dark photon emission rate in a dense medium is $\kappa^2_{{\rm eff},a}\Gamma^{\rm prod}_{A_a}$. The evolution of the total number density of dark photons can be calculated from the Boltzmann equation as

$$\dot{n}_{A'_a} + 3Hn_{A'_a} = \int \frac{d^3\mathbf{k}}{(2\pi)^3}\,\kappa^2_{{\rm eff},a}\,\Gamma^{\rm prod}_{A_a}(\omega) - n_{A'_a}\,{\tau_{A'}}^{-1}, \tag{2.4}$$

JCAP12(2020)049

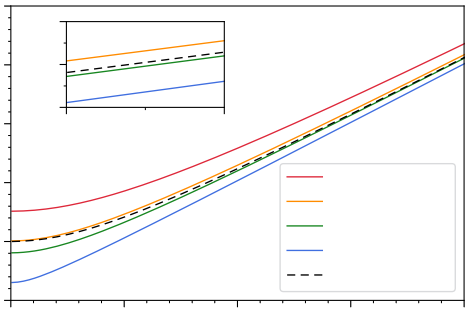

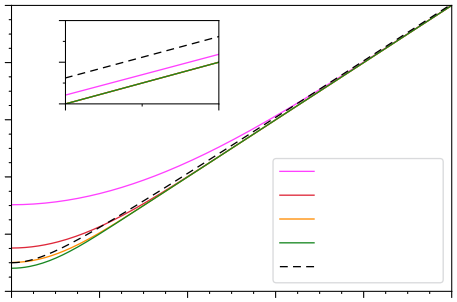

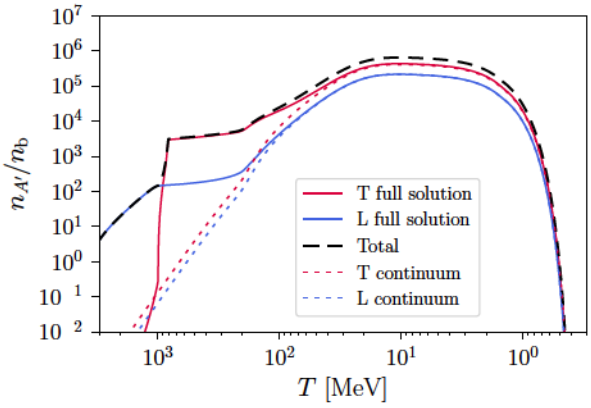

Figure 3. Evolution of the ratio of dark photons to baryons plotted against plasma temperature for a model where $m_{A'} = 100\,\mathrm{MeV}$ and $\kappa = 10^{-10}$. Red (blue) lines give the transverse (longitudinal) mode. For a given mode, dotted lines show the production history if we ignore plasma effects at all temperatures, i.e., $\kappa_{\mathrm{eff,a}} = \kappa$. The result of ignoring the plasma effects gives the continuum contribution. Conversely, solid lines show the complete production history if we include the plasma effects encapsulated in equation (2.2). The dashed black line gives the total number of dark photons for the three modes ($a = \pm\mathrm{T}, \mathrm{L}$) in the full solution. Resonant production within the plasma occurs at early times ($T \gtrsim 8\,m_{A'}$) while continuum production dominates at late times ($T \lesssim m_{A'}$).

temperature regime where $\mathrm{Re}\,\pi_a \gg m_{A'}^2$, the effective coupling reduces to $\kappa {m_{A'}}^4/\mathrm{Re}\,{\pi_a}^2$, so the continuum emission rate is suppressed by a factor ${m_{A'}}^4/\mathrm{Re}\,{\pi_a}^2$ relative to the rate in the low temperature regime [17]. Moreover, there is always more time to produce dark photons at low temperatures than at high temperatures because the Hubble expansion rate in these radiation dominated conditions drops with decreasing temperature, $H \sim T^2/m_{\mathrm{pl}}$ with m_{pl} the Planck mass. As a result, the continuum dark photon production is always more significant at low temperatures than at high temperatures.

We would like to understand the role of the resonant production channel in contributing to the overall dark photon yield, and assess its significance relative to continuum production. As an example, in figure 3 we show the dark photon production history for a specific dark photon mass $m_{A'} = 100\,\mathrm{MeV}$. The solid lines show the full solutions for dark photon emission with in-medium plasma effect included. The solid lines are color coded for longitudinal and transverse modes. On the other hand, the dashed lines show the production histories when no plasma effects are included. The rapid rise in dark photon number density in the temperature range $8\,m_{A'} < T < 10\,m_{A'}$, and at $T > 10\,m_{A'}$, is a consequence of resonant production of transverse and longitudinal modes. These histories agree with those shown in figure 2. For the lepton/quark-pair annihilation production channel, we can conclude from the calculations shown in the figure that longitudinal mode resonant production is insignificant relative to resonant transverse mode production. See, for example, ref. [15] for a discussion of stellar conditions in the regime where the dark photon mass is less than the plasma frequency, $m_{A'} < \omega_{\mathrm{p}}$, and where, consequently, the resonant dark photon emission production of longitudinal modes dominates over the resonant transverse mode production rate. On the other hand, the continuum production rates for both transverse and longitudinal modes are initially small at $T > 10\,m_{A'}$ as a consequence of the extra suppression factor ${m_{A'}}^4/\mathrm{Re}\,{\pi_a}^2$, but these eventually dominate the total dark photon emission when $T \lesssim m_{A'}$. Comparing the full and continuum solutions, we see that: (1) resonant production is important only at $T \gtrsim 8\,m_{A'}$; and (2) eventually the continuum production dominates over the resonant

JCAP12(2020)049

JCAP12(2020)049

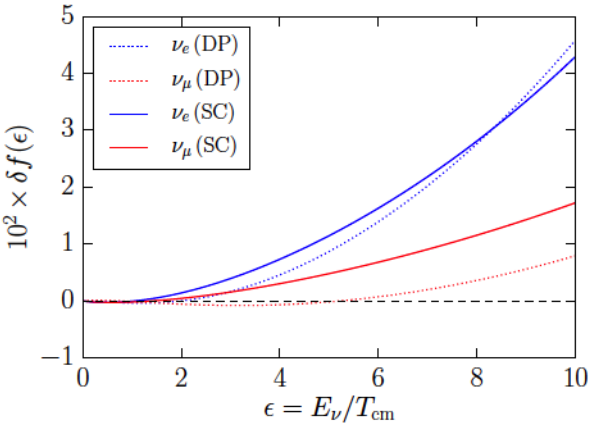

Figure 4. Relative differences from FD [equation (3.7)] for a dark photon model (dotted) and standard cosmology (solid) versus ϵ at freeze-out. The parameters for the dark photon model are $m_{A'} = 10\,\mathrm{MeV}$ and $\kappa = 2 \times 10^{-10}$.

We add $\rho_{A'}$ to the energy densities of the other components to calculate the Hubble expansion rate H. During dark photon production and decay, we assume the energy density of the electromagnetic plasma instantly equilibrates, which induces a change in the plasma temperature time-derivative [40]

$$\frac{dT}{dt} = -3H \frac{\rho_{\rm pl} + P_{\rm pl} + \frac{1}{3H}\frac{dQ}{dt}\Big|_T}{\frac{d\rho_{\rm pl}}{dT}}, \tag{3.3}$$

where $\rho_{\rm pl}$ is the energy density of the plasma (less baryons); $P_{\rm pl}$ is the pressure exerted by all plasma components; $dQ/dt|_T$ is the rate of heat gain or lost from nuclear reactions, neutrino scattering/decoupling, and dark photon evolution; and $d\rho_{\rm pl}/dT$ is the temperature derivative of the plasma energy density components (including baryons). We model the energy subtraction (injection) from dark photon production (decay) using the heat sink (source)

$$\left.\frac{dQ}{dt}\right|_T = -\left.\frac{dQ}{dt}\right|_{\rm nuc} + \left.\frac{dQ}{dt}\right|_\nu - \left.\frac{dQ}{dt}\right|_{A' \leftrightarrow l\bar{l}}, \tag{3.4}$$

$$= -\left.\frac{dQ}{dt}\right|_{\rm nuc} + \left.\frac{dQ}{dt}\right|_\nu + m_{A'}\frac{dn_{A'}}{dt}. \tag{3.5}$$

An injection of heat will raise the entropy per baryon within the plasma $s_{\rm pl}$, which is equivalent to diluting the baryon number density. Therefore, we start with a low entropy-per-baryon and allow the dark photon decays to raise the entropy per baryon (or lower the baryon number density) to a value consistent with photon decoupling, namely $s_{\rm pl} = 5.91 \times 10^9$ [39]. For each dark photon model (set of dark photon mass and coupling parameters), we iterate on the starting entropy to find the final entropy consistent with ref. [39], $s_{\rm pl,cmb}$.

3.2 Neutrino spectra

As the dark photons decay, they inject heat into the electromagnetic plasma. This heat flow changes the temperature of the plasma giving a different thermal history for the early universe as compared to the standard cosmology. For the dark photon masses we consider

JCAP12(2020)049

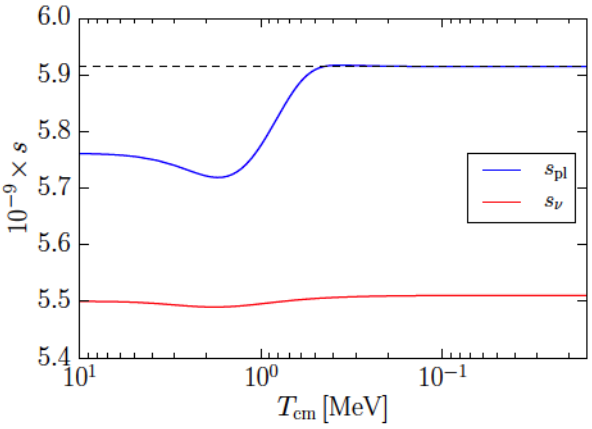

Figure 5. The plasma (blue) and neutrino (red) entropies per baryon versus $T_{\rm cm}$ for a dark photon model. The parameters for the dark photon model are $m_{A'} = 10\,\mathrm{MeV}$ and $\kappa = 2 \times 10^{-10}$. The black dashed line is the entropy per baryon as inferred from the CMB in ref. [39].

in this work, the neutrinos cannot directly partake in this heat flow from dark photon decay. However, a warmer plasma will precipitate a larger heat flow from the plasma into the neutrino seas during neutrino decoupling. As a result, dark photon decays do affect the neutrino spectra indirectly.

As an illustrative example, we take a specific case for dark photon rest mass and coupling to the standard model and calculate in depth how the production and decay of this particle affects weak decoupling and entropy flow. In particular, we show the neutrino energy spectral distortions and the evolution of entropy in figures 4, 5, and 6. For this example case we choose

$$m_{A'} = 10\,\mathrm{MeV}, \quad \kappa = 2 \times 10^{-10}, \tag{3.6}$$

and use the standard cosmological model (i.e., a zero dark photon density) for a baseline comparison. We have picked this particular dark photon model in equation (3.6) because of the associated large change in the entropy per baryon during neutrino decoupling. Figure 4 shows the relative changes in the occupation number from FD (Fermi-Dirac) equilibrium

$$\delta f(\epsilon) = \frac{f(\epsilon) - f^{(\mathrm{eq})}(\epsilon)}{f^{(\mathrm{eq})}(\epsilon)}, \quad f^{(\mathrm{eq})}(\epsilon) = \frac{1}{e^{\epsilon} + 1}, \tag{3.7}$$

plotted against the comoving invariant $\epsilon = E_\nu / T_{\rm cm}$, where E_ν is the neutrino energy and $T_{\rm cm}$ is a proxy for (inverse) scale factor [41]. Solid curves give the deviations from FD equilibrium in the case of the standard cosmology, whereas the dotted lines are for the dark photon model in equation (3.6). The blue curves are for the electron-flavor neutrino and the red for μ-flavor. The τ-flavor neutrinos are degenerate with μ-flavor and the antineutrinos are degenerate with the neutrinos in our model of neutrino transport sans oscillations. The black dashed line at zero represents FD equilibrium. The dashed and solid lines deviate from one another, showing two unique histories for neutrino decoupling, one with the dark photon with the assumed parameters, one without.

As the dark photons decay, the entropy increase in the plasma dilutes the neutrino seas and changes the thermal history of the early universe. We show the entropic history for the dark photon decay scenario in figure 5. In this figure, entropy is plotted as a function of the comoving temperature quantity, $T_{\rm cm}$. The blue curve gives the entropy per baryon in

JCAP12(2020)049

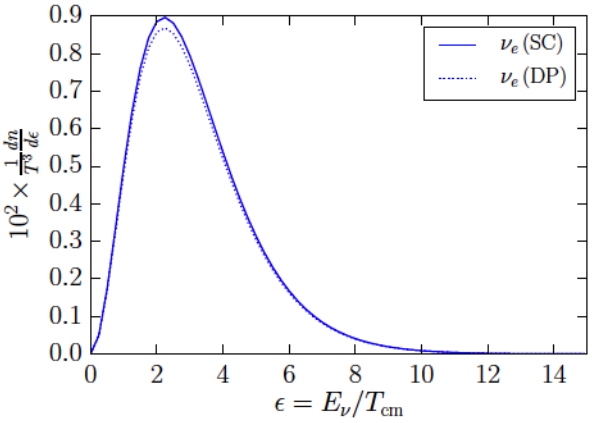

Figure 6. Differential ν_e number densities scaled by plasma temperature [equation (3.11)] for a dark photon model (dotted) and standard cosmology (solid) versus ϵ at freeze-out. The parameters for the dark photon model are $m_{A'} = 10\,\mathrm{MeV}$ and $\kappa = 2 \times 10^{-10}$.

the plasma, $s_{\rm pl}$, and the red curve the entropy per baryon residing in the neutrino seas, s_ν. We calculate the plasma entropy from equilibrium thermodynamics. The neutrino seas are out-of-equilibrium so we calculate that entropy using non-equilibrium statistical mechanics, i.e., Boltzmann neutrino energy transport (see section IV in ref. [34]). Both quantities count the number of microstates available to the two subsystems. The dashed black horizontal line in figure 5 is the entropy-per-baryon inferred from ref. [39]. There is a small increase in s_ν arising from neutrino transport and equivalently encapsulated in the dotted curves of figure 4 at freeze-out. This small increase is accompanied by a small decrease in $s_{\rm pl}$ which is dwarfed by the large increase in the entropy from dark photon decay. The phenomenon of dilution is the increase in the ratio of the entropic quantities from early times to late. The change in the entropy gives a nonstandard thermal history for the early universe. We can summarize the thermal history using the ratio of $T_{\rm cm}$ to T at freeze-out

$$\left.\frac{T_{\rm cm}}{T}\right|_{\rm f.o.} = 0.7082 \quad m_{A'} = 10\,\mathrm{MeV}, \kappa = 2 \times 10^{-10}, \tag{3.8}$$

$$\left.\frac{T_{\rm cm}}{T}\right|_{\rm f.o.} = 0.7138 \quad \text{Standard Cosmology (SC)}. \tag{3.9}$$

Figures 4 and 5 show that the neutrinos experience two competing and opposing effects: an increase in the heat flow from the plasma to the neutrino seas at the level of a few percent deviation (figure 4); and dilution of the neutrino seas at a level of 20% (figure 5). The former effect raises the number of neutrinos at a given energy bin ϵ and $T_{\rm cm}$, which we write as a differential number density

$$\frac{dn_i}{d\epsilon} = T_{\rm cm}^3 \frac{\epsilon^2}{2\pi^2} f_i(\epsilon), \tag{3.10}$$

for a given neutrino flavor i. The later effect decreases the number of neutrinos with respect to photons which we encode in the ratio of $T_{\rm cm}/T$. Figure 6 encapsulates both effects, showing a scaled differential number density

$$\frac{1}{T^3}\frac{dn}{d\epsilon} = \left(\frac{T_{\rm cm}}{T}\right)^3 \frac{\epsilon^2}{2\pi^2} f(\epsilon), \tag{3.11}$$

JCAP12(2020)049

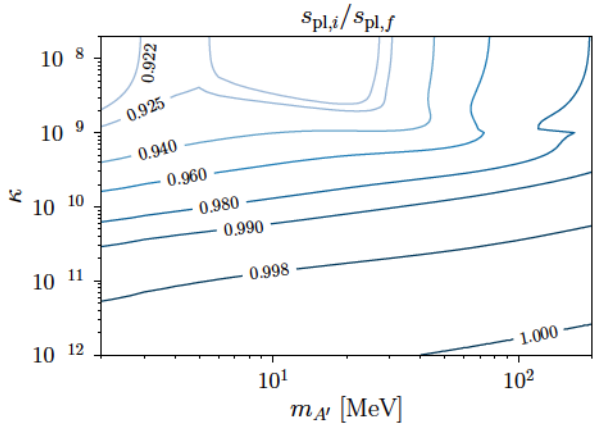

Figure 7. Contours of constant initial-to-final entropy ratios ($s_{\mathrm{pl},i}/s_{\mathrm{pl},f}$) plotted in the κ versus $m_{A'}$ parameter space. The contours with values below 1.0 indicate an increase in entropy due to the dark photon production and decay.

plotted against ϵ. We only plot the scaled differential number densities for electron-flavor neutrinos in the dark photon decay scenario (dotted line) and the standard cosmology (solid line). The μ-flavor quantities are qualitatively identical. The scaled differential number density is a scale-dependent quantity, so we plot figure 6 at the respective freeze-out epochs for each scenario which would occur at different T and T_{cm}.

The previous exposition has delved into the details of neutrino transport with dark photons. For the specific model we considered, the dominant effect on the neutrino number density (and by extension energy density) was dilution. Energy flow from neutrino transport adds on order an 1% increase to the total neutrino energy density. The increase is dependent on the particular model of dark photons. $\mathcal{O}(1\%)$ contributions may be important in future high-precision modeling of BSM cosmologies and we emphasize the need for such calculation if/when the data warrant it. For the purposes of this work, we will focus on dilution when discussing the dark photon parameter space in its entirety, and discuss sub-dominant transport effects for specific models.

3.3 Radiation energy density

The first observable consequence of entropy injection and dilution is decreasing the neutrino radiation energy density (as parameterized by N_{eff}) compared to the value predicted in the standard cosmology. In this subsection, we first calculate the dilution effect in the dark photon model and show the changes in N_{eff} for the full model parameter space; this would be for the case without including energy transport between neutrinos and the plasma. We then discuss the effect of neutrino-energy transport on N_{eff} for a few sets of dark photon model parameters and show the non-linear scaling of the N_{eff} correction with either $m_{A'}$ or κ.

3.3.1 Sharp neutrino decoupling

The energy density of the neutrino seas is solely a function of T_{cm}

$$\rho_\nu = 6\left(\frac{7}{8}\right)\left(\frac{\pi^2}{30}\right)T_{\mathrm{cm}}^4 \tag{3.12}$$

when ignoring out-of-equilibrium contributions. The CMB power spectrum is sensitive to the radiation energy density, ρ_{rad}, of the early universe, which we parameterize using the

JCAP12(2020)049

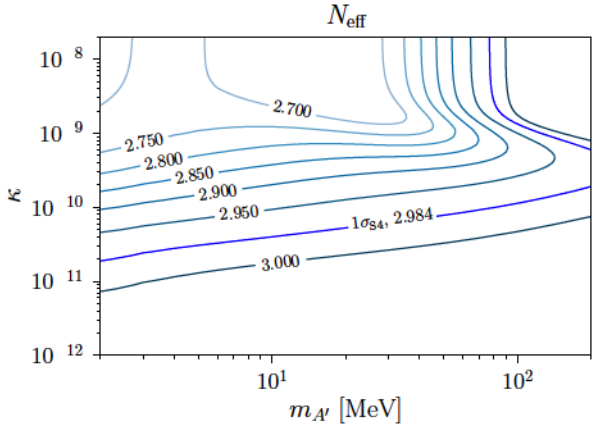

Figure 8. Contours of $N_{\rm eff}$ are shown for values of dark photon mass $m_{A'}$ and mixing parameter κ. For reference, we also plot the QED-only prediction of $N_{\rm eff} = 3.011$ in the absence of neutrino-energy transport. The blue contour is down from 3.011 by $1\,\sigma_{\rm S4}$ where we quote the measurement uncertainty $1\,\sigma_{\rm S4} = 0.027$ from the CMB Stage-4 science book [2].

quantity $N_{\rm eff}$ and plasma temperature T

$$\rho_{\rm rad} = \left[2 + \frac{7}{4}\left(\frac{4}{11}\right)^{4/3} N_{\rm eff}\right]\frac{\pi^2}{30}T^4. \tag{3.13}$$

If we take the radiation energy density to be the sum of the photon and neutrino components, we find

$$N_{\rm eff} = 3\left(\frac{11}{4}\right)^{4/3}\left(\frac{T_{\rm cm}}{T}\right)^4. \tag{3.14}$$

After weak decoupling, dark photon decay injects entropy only into the electromagnetic plasma. This process results in the dilution of both the baryon number and the neutrino energy densities. If $s_{{\rm pl},i}$ is the entropy per baryon in the plasma at an initial epoch, and $s_{{\rm pl},f}$ is the same quantity at a final epoch, then the ratio behaves like the following

$$\frac{s_{{\rm pl},i}}{s_{{\rm pl},f}} = \left(\frac{\frac{2\pi^2}{45}g_{\star S}^{(i)}T_i^3}{\frac{2\pi^2}{45}g_{\star S}^{(f)}T_f^3}\right)\left(\frac{n_{b,f}}{n_{b,i}}\right) = \frac{g_{\star S}^{(i)}}{g_{\star S}^{(f)}}\left(\frac{T_i a_i}{T_f a_f}\right)^3 = \frac{11}{4}\left(\frac{T_{\rm cm}}{T}\right)^3_{\rm f.o.}, \tag{3.15}$$

where we have selected the initial epoch such that $T_{{\rm cm},i} = T_i$ and the final epoch such that the ratio $T_{\rm cm}/T$ has reached a freeze-out value, i.e., all of the plasma entropy resides in SM photons. Figure 7 shows the contours of $s_{{\rm pl},i}/s_{{\rm pl},f}$ in the κ vs. $m_{A'}$ parameter space. All contours are less than or equal to unity, showing that the physics of dark photons precipitates dilution.

If we compare equation (3.15) to equation (3.14) evaluated at freeze-out, we find

$$N_{\rm eff} = 3\left(\frac{s_{{\rm pl},i}}{s_{{\rm pl},f}}\right)^{4/3}. \tag{3.16}$$

As a result, we expect contours of $N_{\rm eff}$ to correspond directly to the contours of $s_{{\rm pl},i}/s_{{\rm pl},f}$ in figure 7. That is, a smaller value of $s_{{\rm pl},i}/s_{{\rm pl},f}$ (a larger dilution effect) would lead to a smaller value of $N_{\rm eff}$ (a more diluted neutrino radiation density). Figure 8 shows the contours of $N_{\rm eff}$ as functions of κ and $m_{A'}$ in the case of dark photon decay. Indeed, the $N_{\rm eff}$ contours do

JCAP12(2020)049

$m_{A'}$ [MeV]	κ	$N_{\rm eff}$ (QED only)	$N_{\rm eff}$ (w/ trans.)	Diff	Diff/$\sigma_{\rm S4}$
SC		3.0113	3.0442	0.0329	1.2201
2.0	1×10^{12}	3.0097	3.0426	0.0329	1.2192
2.0	1×10^{11}	2.9961	3.0289	0.0327	1.2128
2.0	1×10^{10}	2.8944	2.9237	0.0293	1.0834
2.0	1×10^{9}	2.7201	2.7152	-0.0049	-0.1838
2.0	1×10^{8}	2.6934	2.6838	-0.0096	-0.3560
10.0	2×10^{12}	3.0101	3.0430	0.0329	1.2188
10.0	2×10^{11}	2.9983	3.0306	0.0323	1.1970
10.0	2×10^{10}	2.9012	2.9147	0.0135	0.5009
10.0	2×10^{9}	2.7110	2.8807	0.1697	6.2866
10.0	2×10^{8}	2.6656	2.8894	0.2238	8.2284

Table 1. Table of values related to $N_{\rm eff}$. First and second columns are the dark photon mass and coupling, respectively. Third and fourth columns are the value of $N_{\rm eff}$ with only QED effects and with transport included, respectively. Fifth column is the difference between the fourth and third columns. Sixth column is that difference scaled by the uncertainty in $N_{\rm eff}$ as forecast by CMB Stage-4 [2]. The first row gives the values calculated in the standard cosmology with our code.

follow the same general trend of the dilution contours in figure 7. For low $m_{A'}$, a large value of κ induces rapid dark photon production and results in a non-negligible abundance. In addition, peak production occurs in the temperature range $0.1\, m_{A'} \lesssim T_{\rm peak} \lesssim m_{A'}$. For the low end of our mass-range study, peak production occurs after the sharp neutrino decoupling we have instituted for the parameter space scan. This added entropy from dark photon decay dilutes the thermal neutrino seas and lowers $N_{\rm eff}$ to a value smaller than 3. At large κ and $m_{A'} \gtrsim 100\,\text{MeV}$, the dark photons are both created and decay away before neutrino decoupling, and thus there is little or no dilution on the neutrino energy density. The difference in the contour patterns between figures 7 and 8 is a result of how we calculate the initial entropy. We fix the initial epoch at $T = 30\,\text{MeV}$ regardless of $m_{A'}$. For large $m_{A'}$, the entropy is changing in this initial regime and so the respective contours in figure 7 do not meet the criteria used to derive equation (3.16), and hence diverge from the more precise contours of figure 8.

We plot a blue contour at $N_{\rm eff} = 2.984$ on figure 8. This contour uses a $1\,\sigma_{\rm S4} = 0.027$ uncertainty in $N_{\rm eff}$ from a CMB Stage-4 forecast [2]. The $1\,\sigma_{\rm S4}$ difference is between the contour level and the QED-only prediction of $N_{\rm eff} = 3.011$ in the absence of heat flow from neutrino-energy transport [41]. The specific location in the dark-photon parameter space for the $1\,\sigma$ contour would be the same if transport were to add an offset to all of the contour levels, although $N_{\rm eff}$ would take on a value ≈ 3.02 for the $1\,\sigma$ contour in that scenario. However, this procedure relies on the assumption that the effect of transport is independent of the dark photon physics. We expand upon this detail in the following section.

3.3.2 Effects from neutrino energy transport

The contours of figure 8 are for a model of neutrino decoupling which does not include energy transport between neutrinos and charged leptons. In this scenario, the baseline QED-only calculation would yield $\Delta N_{\rm eff} \equiv N_{\rm eff} - 3 = 0.011$, where the departure from exactly three is due to finite-temperature QED effects which change the entropy of the plasma [42, 43] (see

JCAP12(2020)049

JCAP12(2020)049

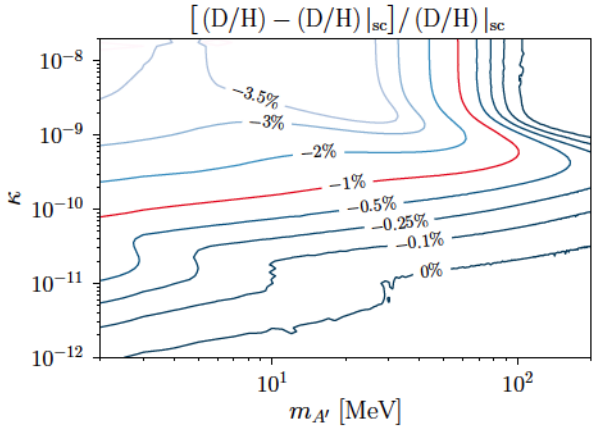

Figure 9. Same parameter space as figure 8, except here we give the percentage change of the primordial deuterium abundance yield in the dark photon model, D/H, as compared to our calculated standard model physics and standard cosmology result, $(\mathrm{D/H})|_{\mathrm{sc}} = 2.64 \times 10^{-5}$. The red contour is down from our standard model value by an assumed 1% uncertainty, i.e., $\sigma = 2.64 \times 10^{-7}$. The coarseness of the contour at 0% is a numerical artifact.

QCD [55], experimental [56], and phenomenological [57–60] sources. The results of those efforts can be integrated into a BBN nuclear reaction network at the appropriate time to yield high-precision absolute BBN predictions. For the dark photon parameter space we study here, we anticipate that changes to D/H from updated reaction networks will not depend on the dynamics of dark photon decay, i.e., the effect of an updated network is to linearly perturb a baseline value. As a result, we give our D/H results as relative differences from a baseline instead of absolute abundance predictions.

Figure 9 shows the contours of primordial deuterium abundance yield as functions of mixing parameter and dark photon mass in the case of dark photon decay. The plot is presented as the percentage change of the primordial deuterium abundance in the dark photon model, D/H, as compared to our calculated standard model and standard cosmology result, $(\mathrm{D/H})|_{\mathrm{sc}} = 2.64 \times 10^{-5}$. At large κ and low $m_{A'}$, dark photons are created abundantly and their decay happens during BBN. That is, the plasma would start out with a lower value of s_{pl} (or higher value of η) at the BBN epoch than in the case of standard cosmology. This alters the final deuterium abundance yield. At large κ and $m_{A'} \gtrsim 100\,\mathrm{MeV}$, dark photons are both created and decay away too early (well before BBN) to have impact on primordial nucleosynthesis.

We use D/H as the diagnostic for BBN in figure 9 because it is well measured and is a priori the most sensitive to changes in entropy. Complementary to D/H, the helium mass fraction, Y_{P}, is also well measured and sensitive to the neutron-to-proton ratio n/p. The rates of the neutron-to-proton inter-conversion processes dictate the evolution of n/p down to low temperatures. These rates are sensitive to the distributions of neutrinos, anti-neutrinos, electrons, and positrons. In particular, four of these rates are sensitive to the dynamics of dark photons, namely

$$\nu_e + n \leftrightarrow p + e^- \tag{3.17}$$

$$e^+ + n \leftrightarrow p + \overline{\nu}_e. \tag{3.18}$$

As dark photons begin to decay, the temperature of the plasma increases. The Pauli blocking factors for the charged leptons suppress the forward rate in equation (3.17) and also the

JCAP12(2020)049

JCAP12(2020)049

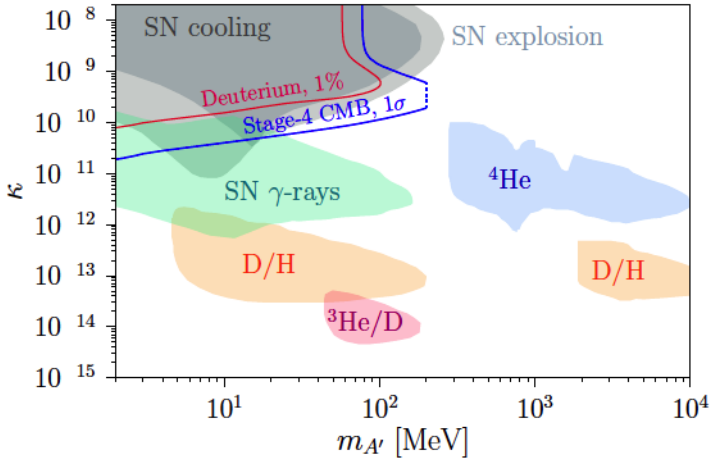

Figure 10. The color-shaded regions show existing bounds on dark photon mass and mixing parameters (as in figures 8 and 9). These bounds, obtained in previous studies, include: SN1987a cooling bound (dark grey) [61]; progenitor envelope bound from core-collapse SN (light grey) [62]; non-observation of γ-rays from SN1987a (green) [63]; and BBN bounds derived from photo-dissociation and neutron excess (orange, red, blue) [25]. (Note the D/H and ^{3}He/D bounds have been updated in ref. [26].) Dark photon parameters lying along the blue line give deviations in $N_{\rm eff}$ which are $1\,\sigma_{\rm S4}$ (where the uncertainty is the CMB Stage-4 science book value, $1\,\sigma_{\rm S4} = 0.027$) below our baseline SC-calculated result with neutrino transport, $N_{\rm eff} = 3.044$. Likewise, the red line shows the dark photon parameters giving a 1% deviation of our calculated deuterium yield from our standard model and standard cosmology result, $10^5 \times ({\rm D/H})\,|_{\rm sc} = 2.64$. The blue dotted line denotes the location of the upper value of the dark photon mass range, $2\,{\rm MeV} \leq m_{A'} \leq 200\,{\rm MeV}$, studied in this work.

is due to the uncertainties in our nuclear reaction network which we do not claim as a source of tension. This source of uncertainty restricts us from making constraints on the model parameters with the absolute value of D/H. However, we project that uncertainties from the nuclear reaction network will be overcome in the near future (as discussed in section 3.4) and that the D/H from the standard model physics and standard cosmology calculation can eventually be directly compared to the observations. Under that assumption, we can make a *potential* bound by applying an assumed 1%-level uncertainty to the deuterium abundance yield in our calculation: for the model parameters circled by the red contour line (i.e., the region at the top-left portion of figure 10), the predicted primordial deuterium abundance with the indicated dark photon parameters is under-produced, that is, down by more than 1% from our standard model value. Hence, these dark photon parameters could be potentially ruled out.

We note that while our potential deuterium bound overlaps with the existing supernova bounds [61, 62], it is obtained from a self-consistent treatment of weak decoupling and BBN physics in the early universe environment. Therefore, our result provides a complementary verification of the supernova bounds derived from the stellar cooling argument.

In figure 10, we also show the existing constraints on the dark photon model as the various color-shaded regions. The dark grey region, labeled as "SN cooling", is the bound derived from the anomalous cooling of SN1987a due to the emission of dark photons [61]. The light grey region, labeled as "SN explosion", is the bound derived from the energy deposition in the progenitor stellar envelopes via emission of dark photons in the proto-neutron star core [62]. The green region shows the bound on the non-detection of gamma-rays, which are

JCAP12(2020)049

JCAP12(2020)049

JCAP12(2020)049

JCAP12(2020)049

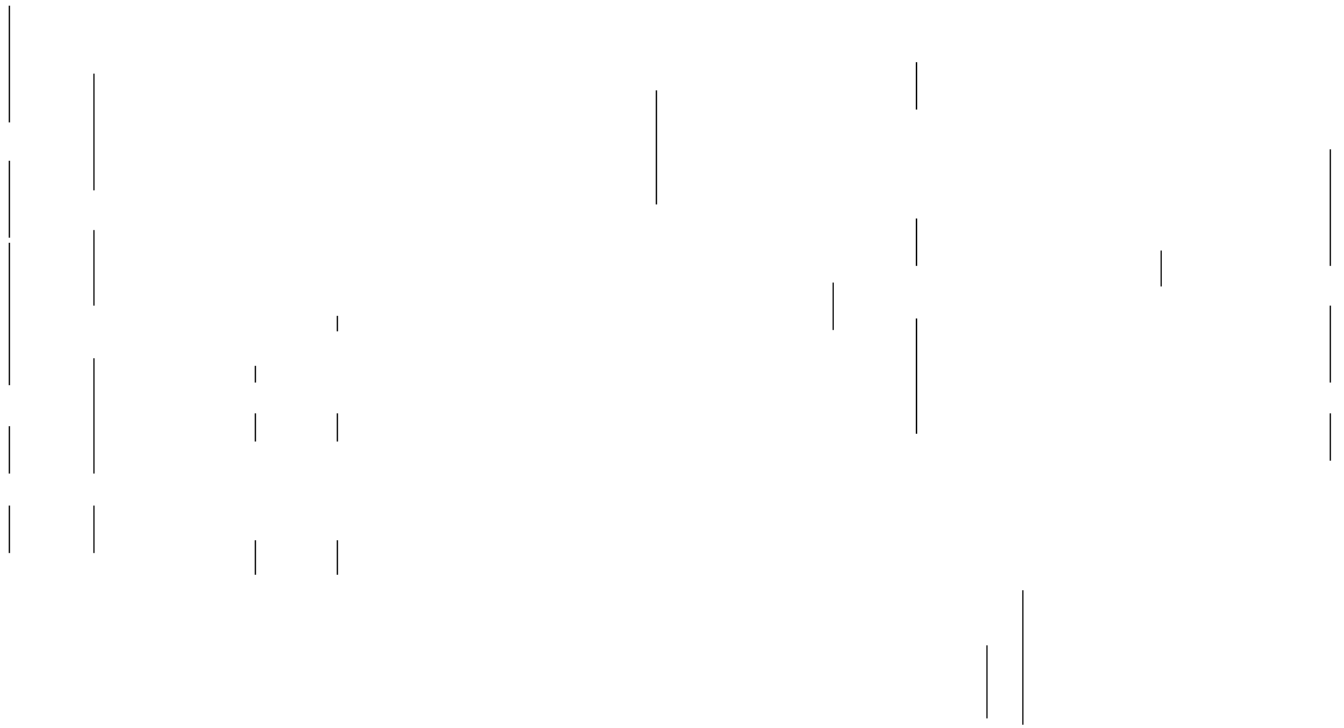

B In-medium effect to dark photon couplings

The effective couplings of a massive dark photon depends strongly on the properties of SM photon polarization in the dense medium. In this appendix we review the in-medium Lagrangian and the conditions required for resonant dark photon emission [66].

The self energy of the photon field A^μ in a dense medium is described by including an additional potential term $-\frac{1}{2}A_\mu \Pi^{\mu\nu} A_\nu$ in the vacuum Lagrangian in equation (1.1). After making a field redefinition $A_\mu \to A_\mu + \kappa A'_\mu$ to rotate away the kinetic mixing term, the in-medium Lagrangian of the relevant terms to $\mathcal{O}(\kappa)$ becomes

$$\begin{aligned}\mathcal{L}_{\rm IM} \supset & -\frac{1}{4}F_{\mu\nu}F^{\mu\nu} - \frac{1}{4}F'_{\mu\nu}F'^{\mu\nu} + \frac{1}{2}{m_{A'}}^2 A'_\mu A'^\mu \\ & - \frac{1}{2}A_\mu \Pi^{\mu\nu} A_\nu - \kappa A_\mu \Pi^{\mu\nu} A'_\nu + e(A_\mu + \kappa A'_\mu) J^\mu_{\rm em}.\end{aligned} \tag{B.1}$$

Next, we project the photon and dark photon fields onto transverse ($\pm$T) and longitudinal (L) directions and consider only one polarization at a time. This can be done by decomposing a given vector field V^μ into its three polarization states as

$$V^\mu = \sum_{a=\pm{\rm T},{\rm L}} V_a \hat{e}^\mu_a \equiv \sum_{a=\pm{\rm T},{\rm L}} V^\mu_a, \tag{B.2}$$

where again each basis vector satisfies $\hat{e}_a{}^\mu \hat{e}_{a,\mu} = -1$. As a result, the in-medium Lagrangian of one given single polarization state a is

$$\begin{aligned}\mathcal{L}_{{\rm IM},a} \supset & -\frac{1}{4}F_{a,\mu\nu}F_a^{\mu\nu} - \frac{1}{4}F'_{a,\mu\nu}F'^{\mu\nu}_a + \frac{1}{2}{m_{A'}}^2 A'_{a,\mu}A'^\mu_a \\ & + \frac{1}{2}\pi_a A_{a,\nu}A^\nu_a + \kappa\pi_a A_{a,\mu}A'^\mu_a + e(A_{a,\mu} + \kappa A'_{a,\mu})J^\mu_{\rm em}.\end{aligned} \tag{B.3}$$

The mixing between the photon and dark photon fields can be rotated away by making another field redefinition,

$$\begin{aligned}A_{a,\mu} &= \tilde{A}_{a,\mu} + \frac{\kappa\pi_a}{m^2_{A'} - \pi_a}\tilde{A}'_{a,\mu}, \\ A'_{a,\mu} &= \tilde{A}'_{a,\mu} - \frac{\kappa\pi_a}{m^2_{A'} - \pi_a}\tilde{A}_{a,\mu}.\end{aligned} \tag{B.4}$$

Eventually, we arrive at the in-medium Lagrangian of the polarization state a presented in the mass basis as[1]

$$\begin{aligned}\mathcal{L}_{{\rm IM},a} \supset & -\frac{1}{4}\tilde{F}_{a,\mu\nu}\tilde{F}^{\mu\nu}_a - \frac{1}{4}\tilde{F}'_{a,\mu\nu}\tilde{F}'^{\mu\nu}_a + \frac{1}{2}{m_{A'}}^2 \tilde{A}'_{a,\mu}\tilde{A}'^\mu_a \\ & + \frac{1}{2}\pi_a \tilde{A}_{a,\nu}\tilde{A}^\nu_a + e\left(\tilde{A}_{a,\mu} + \frac{\kappa m^2_{A'}}{m^2_{A'} - \pi_a}\tilde{A}'_{a,\mu}\right)J^\mu_{\rm em}.\end{aligned} \tag{B.5}$$

It is clear from equation (B.5) that the effective coupling between $\tilde{A}'_a$ and $J_{\rm em}$ is

$$e\kappa_{{\rm eff},a} = \frac{e\kappa {m_{A'}}^2}{\sqrt{({m_{A'}}^2 - {\rm Re}\,\pi_a)^2 + ({\rm Im}\,\pi_a)^2}}, \tag{B.6}$$

and the dark photon emission rate will be enhanced when ${\rm Re}\,\pi_a$ approaches ${m_{A'}}^2$.

[1] We note that the form of effective kinetic mixing presented in equation (B.5) works for all three polarization states since they satisfy the same form of normalization, $\hat{e}^\mu_a \hat{e}_{a,\mu} = 1$.

JCAP12(2020)049

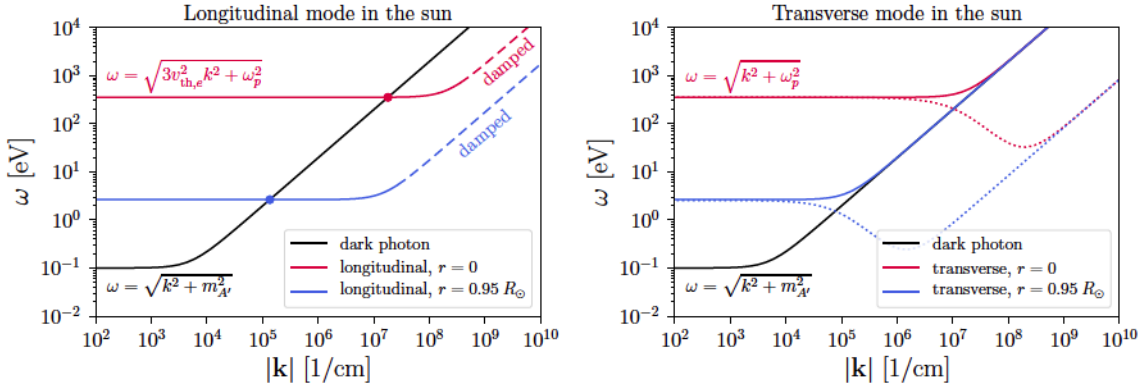

Figure 11. Dispersion relations for the transverse (*right*) and longitudinal (*left*) modes of SM photons in the sun. (*Left*) The red and blue solid curves denote the dispersion relations of the longitudinal mode at the center and at the edge of the sun, respectively. The black curve shows the dispersion relation for a dark photon in a model with $m_{A'} = 10^{\ 1}\,\mathrm{eV}$. Dark photon resonant emission can occur when the SM photon longitudinal dispersion curve intersects the dark photon dispersion curve. This can happen for the range of $|\mathbf{k}|$ values bounded between the intersection points (circles) on the red and blue curves. We note that the longitudinal plasma wave for $|\mathbf{k}| \gtrsim 1/\lambda_{\mathrm{D}}$ in a nonrelativistic plasma suffers strong Landau damping as shown by the dashed lines. (*Right*) The colored solid curves denote the dispersion relations for the transverse mode in the sun. The red (blue) dotted curve is the difference between red (blue) solid curve and the black dark photon curve for each $|\mathbf{k}|$ value. The dispersion relation curve for SM photons in the transverse mode never intersects the dispersion relation curve for a dark photon.

B.1 Example: resonant dark photon emission in a nonrelativistic plasma

References [10, 14, 15] have pointed out the importance of plasma effects in the dark photon emission rate in the sun and in horizontal branch stars when $m_{A'} < 10\,\mathrm{eV}$. Here we use the plasma dispersion relation to interpret these results.

In compact objects, the electron plasma frequency is many orders of magnitude higher than electron cyclotron frequency. As far as the ordinary electromagnetic (transverse) and electrostatic (longitudinal) modes are concerned, the plasma in such conditions can be treated as unmagnetized and isotropic. A SM photon propagating in this environment would then acquire an effective in-medium mass, $\mathrm{Re}\,\pi_a$, where the general form of π_a is given in equations (A.4) and (A.5). With the presence of a dark photon with mass $m_{A'}$, dark photon resonant emission occurs when ${m_{A'}}^2 = \mathrm{Re}\,\pi_a$. This statement is equivalent to saying that the resonance happens when there is a solution of $(\omega, \mathbf{k})$ that satisfies both the dispersion relations for the dark photon, $\omega^2 = |\mathbf{k}|^2 + m_{A'}^2$, and for in-medium SM photons, $\omega^2 = |\mathbf{k}|^2 + \mathrm{Re}\,\pi_a\,(\omega, \mathbf{k})$. While these two dispersion relations are similar in structure, they dictate quite different behavior in a nonrelativistic plasma such as that in the sun or in horizontal branch stars.

In figure 11, we take the sun as an example of the nonrelativistic plasma environment and show the dispersion relations for in-medium photons and for a dark photon. We consider a range of radius r from the center of the sun to 95% of the solar radius, $r \leq 0.95\,R_\odot$. Electrons and protons in the sun are nonrelativistic. The dispersion relation for longitudinal EM oscillation in such an environment is $\omega \approx \omega_{\mathrm{p}}$ when $|\mathbf{k}| \lesssim 1/\lambda_{\mathrm{D}}$, where λ_{D} denotes Debye screening length. This behavior is evident for the solid lines in the left plot of figure 11. When $m_{A'}$ is less than the plasma frequency at around the edge of the sun, $\omega_{\mathrm{p}}|_{r=0.95R_\odot} \sim 1\,\mathrm{eV}$, the dispersion relation curve for the longitudinal EM oscillation may cross the dispersion

JCAP12(2020)049

arXiv:1607.02797 SPIRE

arXiv:1610.02743 SPIRE

arXiv:1310.3163 SPIRE

arXiv:1607.03900

SPIRE

SPIRE

SPIRE

hep-ph/0305261 SPIRE

arXiv:0810.0713 SPIRE

arXiv:0811.1030 SPIRE

arXiv:0801.1527 SPIRE

arXiv:0811.0326 SPIRE

arXiv:0804.4157 SPIRE

arXiv:0901.0014 SPIRE

arXiv:1305.2920 SPIRE

arXiv:1302.3884 SPIRE

arXiv:1507.02614 SPIRE

arXiv:1611.05852 SPIRE

arXiv:1803.07048 SPIRE

arXiv:1904.10567 SPIRE

arXiv:1911.05086 SPIRE

arXiv:2003.13698 SPIRE

arXiv:2002.05165 SPIRE

arXiv:2004.06733 SPIRE

arXiv:2009.03899 SPIRE

arXiv:1407.0993 SPIRE

arXiv:1605.07195 SPIRE

arXiv:1205.3785 SPIRE

arXiv:1308.3240 SPIRE

arXiv:2006.14803 SPIRE

arXiv:1809.01179 SPIRE

arXiv:2003.02273 SPIRE

arXiv:1808.09324 SPIRE

arXiv:1110.6479 SPIRE

arXiv:1512.02205 SPIRE

hep-ph/9302213 SPIRE

SPIRE

arXiv:1807.06209 SPIRE

arXiv:1706.03391 SPIRE

SPIRE

hep-ph/9702324 SPIRE

eff
arXiv:1911.04504 SPIRE

hep-ph/9703315
SPIRE

hep-ph/0506164
SPIRE

arXiv:1212.6943 SPIRE

arXiv:1606.06986 SPIRE

eff
arXiv:2001.04466
SPIRE

arXiv:2008.01074 SPIRE

arXiv:2005.07047

eff arXiv:1912.12152 SPIRE

arXiv:1511.03843 SPIRE

arXiv:1510.07877 SPIRE

arXiv:1505.02422 SPIRE

arXiv:1707.07952 SPIRE

arXiv:1608.05853 SPIRE

arXiv:1710.01647
SPIRE

arXiv:1901.04857
SPIRE

arXiv:1611.03864 SPIRE

arXiv:1903.07923 SPIRE

arXiv:1901.08596
SPIRE

arXiv:1710.11129 SPIRE

arXiv:1903.09187 SPIRE

PoS(TASI2018)009 arXiv:1904.07915
SPIRE

JCAP12(2020)049